Simulation of Time-Dependent Pool Shape during Laser Spot Welding: Transient Effects

GEORG EHLEN, ANDREAS LUDWIG, and PETER R. SAHM

The shape and depth of the area molten during a welding process is of immense technical importance. This study investigates how the melt pool shape during laser welding is influenced by Marangoni convection and tries to establish general qualitative rules of melt pool dynamics. A parameter study shows how different welding powers lead to extremely different pool shapes. Special attention is paid to transient effects that occur during the melting process as well as after switching off the laser source. It is shown that the final pool shape can depend strongly on the welding duration. The authors use an axisymmetric two-dimensional (2-D) control-volume-method (CVM) code based on the volume-averaged two-phase model of alloy solidification by Ni and Beckermann[1] and the SIMPLER algorithm by Patankar.[2] They calculate the transient distribution of temperatures, phase fractions, flow velocities, pressures, and concentrations of alloying elements in the melt and two solid phases (peritectic solidification) for a stationary laser welding process. Marangoni flow is described using a semiempirical model for the temperature-dependent surface tension gradient. The software was parallelized using the shared memory standard OpenMP.

I. INTRODUCTION

IN recent years, great effort has been made to predict the formation of different pool shapes that occur in conduction mode welding. Many research groups have developed sophisticated models that are able to describe the complex interaction of surface tension forces, electromagnetic forces, turbulence, heat losses by radiation, air convection, and evaporation. A short overview is given in Winkler *et al.*[3] Most welding applications include moving heat sources. For these applications, numerical steady-state solutions yield the most interesting information. For welding problems with stationary heat source instead, the numerical steady-state solutions, *e.g.*, References 4 through 8, only give part of the information that might be useful. Some recent works investigate the transient behavior of weld pools, but do not take into account the transient processes after switching off the heat source, *e.g.*, References 3 and 9.

Many experimental and theoretical articles have been published concerning the description and prediction of pool shapes. So the pool shapes shown here, especially V and W shapes, have been experimentally observed and are well known in the literature, *e.g.*, References 3, 8, and 10. But, in general, the formation of the different shapes is explained and interpreted as a function of the concentration of surface-active elements such as sulfur or oxygen. Pitscheneder *et al.*[11] investigate the question why the splitting into flat pools for low sulfur contents and deep pools for high sulfur contents happens at high welding powers and not at low ones. They state that the reason is competition between conductive and convective heat transfer as well as the temperature dependence of surface tension coefficients.

The present numerical study systematically investigates the influence of welding power and welding duration on the formation of pool shapes during laser welding processes using the model for temperature-dependent surface tension gradients by Sahoo *et al.*[12] Special attention is paid to the description of transient effects that in general are neglected by stationary calculations and that can significantly influence the final pool shape. These effects should be considered during the interpretation of experimentally observed weld pools.

The study does not want to give quantitative recipes for specific materials or configurations. The aim is rather to give an overview of the different types of weld pool dynamics that can occur in laser welding systems and to provide a deep understanding of the evolution of weld pools under different welding conditions, how certain pool shapes form, and which effects influence the time-dependent and final pool shape. Stress is laid on establishing general rules of melt pool behavior, without taking into account that the parameters might not always represent realistic welding conditions for the specific system described. In many cases, it may not be possible to realize all the effects.

The behavior and effects observed with the system investigated in this article (Fe 0.42 wt pct C with 0.014 wt pct S) are so general that they should occur in many systems. It gives an idea how variations of parameters such as welding power, welding duration, amount of surface active elements, or even imperfect knowledge of physical constants such as the standard heat of adsorption ΔH^0 can influence the welding results. On the other hand, it becomes obvious which parameters must vary to reach a certain result. If the general rules are to be applied to a specific system, it will be necessary to carry out systematic experimental studies to determine material data, critical temperatures, *etc.* The present study gives the theoretical

GEORG EHLEN, formerly Ph.D. Student with the Foundry Institute, Aachen University, D-52056 Aachen, Germany, is now Research Scientist with Schott Glas, D-55122 Mainz, Germany. Contact e-mail: g.ehlen@web.de ANDREAS LUDWIG, Professor, formerly with the Foundry Institute, Aachen University, is with Metallurgical Processes, Department of Metallurgy, University of Leoben, A-8700 Leoben, Austria. PETER R. SAHM, Professor, is with the Foundry Institute, Aachen University.

Manuscript submitted April 29, 2002.

background on how to do the experiments, and what to search for.

Section II introduces the mathematical and numerical model, the set-up used for the calculations, definitions, and preliminary calculations. Section III presents the results and discussion of the numerical study on transient weld pool behavior. Section IV establishes the general rules extracted from the numerical study. The publication is based on a presentation held at the *6th Int. Sem. on the Numerical Analysis of Weldability*, Graz, Austria, October 1–3, 2001.

II. MODEL DESCRIPTION, DEFINITIONS, AND PRELIMINARY CALCULATIONS

Because the main focus of this article is meant to be on parameter studies and calculation results, the description of the mathematical model and numerical implementation will be kept as short as possible. This section will only give an overview of the implemented submodels and algorithms. The Marangoni model will be discussed in more detail because the knowledge about the behavior of the surface tension gradient as a function of temperature and concentration of surface-active elements is important to understand and interpret the wide area of validity of the results.

The axisymmetric two-dimensional (2-D) model used in this article is based on the volume-averaged two-phase model of alloy solidification suggested by Ni and Beckermann.[1] The microscopic conservation equations have been integrated over a representative "averaging volume" to yield a set of macroscopic equations for the fully coupled calculation of fluid flow and heat and solute transport. The following simplifying assumptions were made:

1. stationary solid phase,
2. Boussinesq approximation in the description of thermosolutal convection,
3. thermodynamic equilibrium, and
4. full solute mixture inside the averaging volume.

The system of nonlinear differential equations has been discretized using an implicit control-volume-method (CVM) and is solved using the SIMPLER algorithm proposed by Patankar.[2]

A phase change algorithm that is based on an iterative scheme presented by Prakash and Voller[13] and Schneider and Beckermann,[14] but has been essentially extended by the authors,[15] uses an energy equation and liquid concentration equation to model eutectic or peritectic remelting and solidification of binary alloys (FeC, AlSi) described by piecewise linear phase diagrams. The lever rule is applied to calculate the local concentration of solute in the liquid phase and to model the formation of macrosegregations. The mushy zone is assumed to be a dendritic network. The reduced permeability of the mushy zone is modeled by an anisotropic permeability tensor that uses the angle of dendrite growth given by the local temperature gradient.[14]

Boundary conditions at the surfaces can describe

1. heat input by a gauss-shaped welding source;
2. heat losses by evaporation, radiation, and air convection; and
3. surface tension driven Marangoni flow.

The Fortran 90 code was parallelized using the shared memory standard OpenMP (version 1.1). The problem structure of multiple nested iteration loops makes parallelization difficult. In addition, the fine-grained structure of the problem—the domain size is 60×40 cells only—limits parallelization efficiency and scalability. On two processors, a speedup of 1.6 is achieved (efficiency: 80 pct). On four processors the speedup rises to 2.6, but efficiency drops to 65 pct. As the parameter studies required a large number of calculations, several of them were run at the same time instead of running them on eight processors on low efficiency (36 pct).

A. *Conservation Equations*

In our approach, three phases are considered, one liquid and two stationary solid phases (liquid: l, solid-delta: δ, and solid-gamma: γ). The following conservation equations are solved: conservation of mass for l, δ, and γ; conservation of r and z momentum and species for l; and conservation of mixture enthalpy. The corresponding equations are as follows:

$$\frac{\partial}{\partial t}(\varepsilon_l \rho_l) + \vec{\nabla}(\varepsilon_l \rho_l \vec{v}_l) = -\Gamma_{\delta l} - \Gamma_{\gamma l} \qquad [1a]$$

$$\frac{\partial}{\partial t}(\varepsilon_\delta \rho_\delta) = \Gamma_{\delta l} \text{ and } \frac{\partial}{\partial t}(\varepsilon_\gamma \rho_\gamma) = \Gamma_{\gamma l} \qquad [1b]$$

$$\frac{\partial}{\partial t}(\varepsilon_l \rho_l \vec{v}_l) + \vec{\nabla}(\varepsilon_l \rho_l \vec{v}_l \otimes \vec{v}_l) = -\varepsilon_l \vec{\nabla} p + \vec{\nabla} \otimes \bar{\bar{\tau}}_l + \varepsilon_l \rho_l \vec{g} + \vec{M}_l^{\Gamma} + \vec{M}_l^{d} \qquad [2a]$$

$$\text{with } \bar{\bar{\tau}}_l = \mu_l \left\{ \vec{\nabla}(\varepsilon_l \vec{v}_l) + \left[\vec{\nabla}(\varepsilon_l \vec{v}_l) \right] t \right\} \qquad [2b]$$

$$\frac{\partial}{\partial t}(\varepsilon_l \rho_l C_l) + \vec{\nabla}(\varepsilon_l \rho_l \vec{v}_l C_l) = \vec{\nabla}(\varepsilon_l \rho_l D_l \vec{\nabla} C_l) + J_l^{\Gamma} \qquad [3]$$

$$\left(\varepsilon_l \rho_l \frac{\partial h_l}{\partial T} + \varepsilon_\delta \rho_\delta \frac{\partial h_\delta}{\partial T} + \varepsilon_\gamma \rho_\gamma \frac{\partial h_\gamma}{\partial T} \right) \frac{\partial T}{\partial t} + \left(\varepsilon_l \rho_l \frac{\partial h_l}{\partial T} \right) \vec{v}_l \cdot \vec{\nabla} T = -\vec{\nabla} q_{l+\delta+\gamma} + S_{l+\delta+\gamma} \qquad [4]$$

where ε_q is the volume fraction, ρ_q the physical density, $\vec{v}_q$ the velocity, τ_q the strain tensor, μ_q the dynamic viscosity, and h_q the enthalpy of phase q; $\vec{q}_q$ he heat flux in phase q, C_q the mass fraction, and D_q the diffusivity of the solute in phase q; $\vec{g}$ is the gravitation vector and p the pressure; $\Gamma_{\delta l}$ and $\Gamma_{\gamma l}$ are the mass transfer rates for the transitions from δ to l and γ to l, respectively; $\Gamma_{l\delta} = -\Gamma_{\delta l}$ and $\Gamma_{l\gamma} = -\Gamma_{\gamma l}$ are those for the opposite transitions (solidification of δ and γ); $\vec{M}_l^{\Gamma}$ accounts for momentum transfer caused by phase change and $\vec{M}_l^{d}$ for momentum loss due to friction or the drag between the liquid and the (stationary) solid; J_l^{Γ} is the species transfer rate, which accounts for the solute redistribution due to solidification (and melting); and $S_{l+\delta+\gamma}$ is the latent heat of fusion. The heat flow in the melting or solidifying material is considered to be independent of the local phase distribution, and is therefore described by a single heat flux approach $\vec{q}_{l+\delta+\gamma} = \lambda_{l+\delta+\gamma} \vec{\nabla} T$, where

$\lambda_{l+\delta+\gamma}$ is the corresponding average heat conductivity $\lambda = \varepsilon_l\lambda_l + \varepsilon_\delta\lambda_\delta + \varepsilon_\gamma\lambda_\gamma$.

Section B–1 through 4 give further details on the source and exchange terms.

B. Source and Exchange Terms

1. Mass Transfer, Phase Change Algorithm

The mass-transfer rates from l to δ or γ are determined using an iterative scheme presented by Prakash and Voller[13] and Schneider and Beckermann[14]. For a single-phase transition (δ or γ melting and solidification), the discretized enthalpy equation and liquid species conservation equation can be written as $T = T(\varepsilon_s)$ and $C_l = C_l(\varepsilon_s)$. The assumption of thermodynamic equilibrium within an averaging volume, $T = T_{liq}$ (C_l), yields the third equation needed to calculate T, C_l, and ε_s. For the eutectic or peritectic solidification, we have $T = T(\varepsilon_\delta,\varepsilon_\gamma)$ and $C_l = C_l(\varepsilon_\delta,\varepsilon_\gamma)$. The conditions at the eutectic/peritectic plateau yield the fourth equation to solve the fourth variable: $C_l = C_{l\,\mathrm{eut/peri}}$ and thus $T = T_{liq}$ $(C_{l\,\mathrm{eut/peri}}) = T_{\mathrm{eut/peri}}$. The set of three or four equations is solved by a Newton–Raphson iteration scheme. Knowing the changes in ε_δ or ε_γ during the corresponding time-step, the mass-transfer rates $\Gamma_{\delta l}$ and $\Gamma_{\gamma l}$ can be calculated by Eqs. [1a] and [1b] and thus used in Eqs. [2] through [4]. The practical implementation of this phase change algorithm for (eutectic/peritectic) the case of welding processes with strong convection and extensive solute transport and considering complete eutectic or peritectic piecewise linear binary phase diagrams requires a considerable numerical effort. The implementation details have been described in Ehlen *et al.*[15] The algorithm was tested with several set-ups that included extreme temperature gradients, high flow velocities, and strong segregation effects. It turned out to be stable for arbitrary paths inside the phase diagram. Figure 1 shows an example of a complex melting and solidification path influenced by convective concentration drift.

2. Momentum transfer

For the momentum transfer due to phase change, the following approach is used:

$$\vec{M}_l^{\Gamma} = \vec{v}_l \sum_{q=\delta\cdot\gamma} \left\{ \max\left[-\frac{\partial \varepsilon_q}{\partial t}, 0 \right] \cdot \rho_q - \varepsilon_q \frac{\partial \rho_q}{\partial t} \right\} \qquad [5]$$

$$= \vec{v}_l \sum_{q=\delta\cdot\gamma} \begin{cases} -\dfrac{\partial(\varepsilon_q\rho_q)}{\partial t} \text{ melting} \left(\dfrac{\partial \varepsilon_q}{\partial t} < 0\right) \\ -\varepsilon_q \dfrac{\partial \rho_q}{\partial t} \text{ solidification} \left(\dfrac{\partial \varepsilon_q}{\partial t} > 0\right) \end{cases}$$

In the case of stationary solid phase, this term must be different for solidification and remelting. Solidifying mass settling on the stationary solid is stopped and its momentum gets lost. This does not alter the velocity of the fluid. Remelting solid has to be accelerated to the average velocity in the cell. In this case, the velocity of the fluid decreases. If this asymmetry is not considered, solidification can lead to high non-physical pore velocities in areas where the liquid fraction is about to disappear.

The choice of adequate momentum exchange terms between the dendritic network and the flowing melt is the subject of ongoing scientific discussions. In our article, we use Darcy's law[14]:

$$\vec{M}_l^d = -\varepsilon_l^2 \mu_l K^{(2)^{-1}} \vec{v}_l \qquad [6a]$$

with

$$K^{(2)^{-1}} = \begin{bmatrix} \dfrac{\cos^2\varphi}{K_{\xi\xi}} + \dfrac{\sin^2\varphi}{K_{\eta\eta}} & \sin\varphi\cos\varphi\left(\dfrac{1}{K_{\xi\xi}} - \dfrac{1}{K_{\eta\eta}}\right) \\ \sin\varphi\cos\varphi\left(\dfrac{1}{K_{\xi\xi}} - \dfrac{1}{K_{\eta\eta}}\right) & \dfrac{\sin^2\varphi}{K_{\xi\xi}} + \dfrac{\cos^2\varphi}{K_{\eta\eta}} \end{bmatrix} \qquad [6b]$$

where $K_{\xi\xi}$ and $K_{\eta\eta}$ are the permeabilities parallel and normal to the primary dendrite arms of δ or γ, and φ is the angle between the primary dendrite arms and the x-axis. For columnar dendritic solidification the direction denoted by φ points along the temperature gradient, both $K_{\xi\xi}$ and $K_{\eta\eta}$ are assumed to be equal for δ and γ. The permeability model has been mentioned here for completeness. Test calculations using this model and a model with no drag forces at all did not show any important influence on the pool shapes. This may be due to the fact that the mushy zone extends over one cell width only.

3. Species transfer

For solidification, we assume that the solid phase grows by adding a thin solid shell (not necessarily uniform in thickness) from the melt during each time-step. The corresponding decrease of the liquid mass per volume and time is simply Γ_{sl} (for $s = \delta, \gamma$). Therefore, the mass of the species in the liquid per volume and time is reduced by

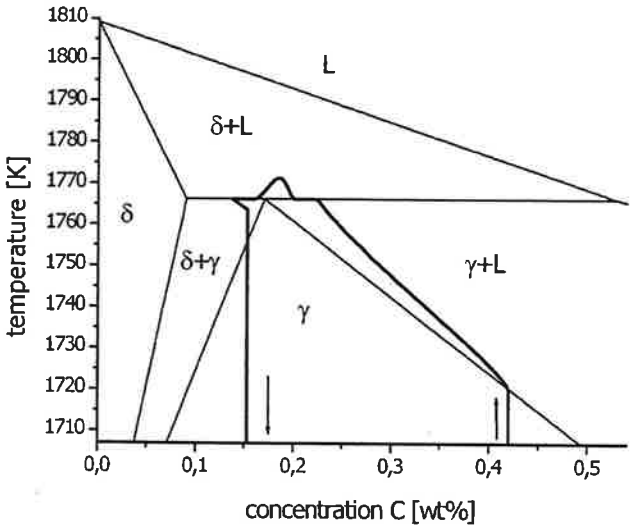

Fig. 1—Concentration drift inside one computational cell in a calculation of a stationary welding process with Fe 0.42 wt pct C. When the cell starts to melt, solute is removed by convection and the mean concentration is reduced. During the primary δ melting, the laser source is switched off and the cell starts to cool. At the end of the peritectic resolidification, the mean concentration of the cell has been reduced so far that some δ phase remains in the solid. The diagonal movement inside the $\delta + \gamma$ area is due to the missing solid-state transformation model.

$C_l\Gamma_{sl}$. From this mass of the species, $k_sC_l\Gamma_{sl}$ is incorporated in the solid (k_s is the equilibrium distribution coefficient of the species in s). Thus, the reduction of liquid mass of the species by $C_l\Gamma_{sl}$ is partly compensated by the amount $(1-k_s)C_l\Gamma_{sl}$, which represents the mass of species not incorporated into the solid shell. In conclusion, we choose the source term of the conservation equation of liquid species mass fraction to be

$$J_l^\Gamma = -k_\delta\, C_l\Gamma_{\delta l} - k_\gamma C_l\Gamma_{\gamma l} \qquad [7]$$

The concentration in delta and gamma solid is assumed to be simply $C_\delta = k_\delta C_l$ and $C_\gamma = k_\gamma C_l$

4. *Heat of fusion*

The source term for the mixture enthalpy conservation equation arises from the enthalpy difference of liquid and delta (heat of fusion for delta formation) and liquid and gamma (heat of fusion for gamma formation):

$$S_{l+\delta+\gamma} = (h_l - h_\delta)\Gamma_{\delta l} + (h_l - h_\gamma)\Gamma_{\gamma l} \qquad [8]$$

C. *Boundary Conditions*

1. *Heat fluxes at the surface of the weld pool*

The heat flux through the surface is a sum of four terms:

$$q_{\text{surface}} = q_{\text{laser}} - q_{\text{radiation}} - q_{\text{convection}} - q_{\text{evaporation}} \qquad [9]$$

The laser heat source is assumed to be Gaussian and can be described as

$$q_{\text{laser}} = q_{\max} \cdot \exp\left(\frac{-2r^2}{r_{\text{laser}}^2}\right) \qquad [10]$$

where $q_{\max}$, the heat flux in the middle of the laser source, is numerically determined in a way that the integral of the heat flux over the entire surface is exactly normalized to the effective input power. The value of r is the distance from the middle of the laser, and r_{laser}, the laser radius, is defined as the radius where the heat flux has decreased to $1/e^2$ of the maximum. The power values used to name the calculations are meant to be effective powers, already including the heat input efficiency η, or assuming η = 100 pct.

Heat losses by radiation and convection are calculated using

$$q_{\text{radiation}} = \varepsilon_b\sigma_b\,(T^4 - T_a^4) \qquad [11]$$

$$q_{\text{convection}} = \alpha_{\text{convection}}\,(T - T_a) \qquad [12]$$

where T is the boundary temperature, T_a the ambient temperature, ε_b the emissivity, σ_b the Stefan–Boltzmann constant, and $\alpha_{\text{convection}}$ the convective heat-transfer coefficient.

In welding processes with high surface temperatures, high vapor pressure plays a major role. To calculate the heat loss by evaporation, a two-step model was implemented: Beneath the evaporation temperature, the heat loss is linked to the temperature-dependent vapor pressure. The model has been described in Zacharia *et al.*[16] The evaporation heat flux is calculated based on an overall vaporization model by Choi *et al.*,[17] given by

$$q_{\text{evaporation}} = W\Delta H_v \qquad [13]$$

where ΔH_v is the heat of evaporation. The equation given by Dushman[18]

$$\log W = A_v + \log p_{\text{atm}} - 0.5 \cdot \log T \qquad [14]$$

is used to calculate the evaporation rate W. The term A_v is a constant that depends slightly on the main components of the alloy used. For the case of a binary FeC alloy, the values of pure iron were taken. The evaporation rate is valid for evaporation into vacuum. Here, we consider evaporation into an atmosphere of 1 bar. The real evaporation rate will therefore be smaller than the one assumed here. Test calculations showed that the qualitative behavior of the pool shapes does not change. To calculate the vapor pressure, an expression given by Kim[19] for stainless steel is used:

$$\log p_{\text{atm}} = 6.1210 - \frac{18{,}836}{T} \qquad [15]$$

If the surface reaches the evaporation temperature, it is assumed that all incoming heat is directly lost by evaporation. The surface temperature is then fixed to this temperature.

2. *Thermal Marangoni convection*

The only surface force considered here is thermal Marangoni convection. This seems to be a good approximation for laser welding. Marangoni convection is driven by local variations of the surface tension γ. Surface tension gradients result in flows toward regions with higher values of γ. Viscosity couples the surface velocity into the fluid and causes convection cells. As surface tension depends on temperature as well as the activities of surface-active elements, two different types, thermal and solutal Marangoni convection, occur. The governing equation describing both effects is

$$\tau_{\text{Mara}} = \mu_l \frac{\partial u}{\partial z} = \frac{\partial\gamma}{\partial T}\cdot\frac{\partial T}{\partial r} + \sum_i \frac{\partial\gamma}{\partial a_i}\cdot\frac{\partial a_i}{\partial r} \qquad [16]$$

where τ_{Mara} is the shear stress caused by surface tension gradients, u the radial velocity component parallel to the surface, r and z the coordinates parallel and perpendicular to the surface, and a_i the thermodynamic activity of alloy element i. As solutal Marangoni convection is in general considered to be much smaller than thermal convection, we have disregarded the solutal effect by assuming the solutal Marangoni coefficients $\partial\gamma/\partial a_i = 0$. In fact, this does not mean that the thermal Marangoni coefficient $\partial\gamma/\partial T$ does not depend on the actual amount of surface-active elements. A semiempirical equation set up by Sahoo *et al.*[12] for binary metal-solute systems gives the following expressions for surface tension and thermal Marangoni coefficient:

$$\gamma(T,a_s) = \gamma_m^0 - A(T - T_m) - R T\Gamma_s \ln(1 + K_{\text{seg}}a_s) \qquad [17]$$

$$\frac{\partial\gamma}{\partial T} = -A - R\Gamma_s \ln(1 + K_{\text{seg}}\,a_s) - \frac{K_{\text{seg}}\,a_s}{1 + K_{\text{seg}}\,a_s}\frac{\Gamma_s\Delta H^0}{T} \quad \text{with} \quad K_{\text{seg}} = S_l\, e^{-(\Delta H^0/(RT))} \qquad [18]$$

Here, γ_m^0 is the surface tension of the pure metal at the melting point, A represents $-\partial\gamma/\partial T$ for the pure metal,

T_m is the melting point of the pure metal, Γ_s is the surface excess of the solute species at saturation, a_s is the activity of the species (in wt pct), ΔH^0 is the standard heat of adsorption, and S_l is a constant that is related to the entropy of segregation. The activity a_S was taken to be equal to the constant concentration of the highly surface-active component sulfur.

In fact, the amount of surface-active elements and the standard heat of adsorption ΔH^0 have a great influence on the value of the Marangoni coefficient. Figure 2(a) shows the temperature-dependent Marangoni coefficient for different values of ΔH^0 and a_S, and Figure 2(b) shows how the critical temperature, defined as the temperature where the Marangoni coefficient changes its sign, depends on the sulfur activity a_S. As a result, the correct knowledge of these parameters is crucial even for qualitatively correct calculations. With increasing sulfur concentration, the critical temperature rises, but qualitatively, the temperature dependence of $\partial\gamma/\partial T$ does not change very much. For this reason, our calculations have been limited to one fixed pair of the parameters $\Delta H^0 - 1.88 \times 10^8$ J/mol and $a_S = 0.014$. These values and the values for all other constants have been determined by Choo *et al.*[6] for the industrial steel AISI 304. The qualitative results can be transferred to cases with different sulfur activities by adapting the welding powers.

The Marangoni forces have been numerically implemented in the form of a velocity source term in the cells close to the surface.

D. *Set-up for the Calculations*

The set-up used for the calculations (Figure 3) is a stationary welding process on an infinite 6-mm steel plate. A cylindrical section of this plate with a radius of 9 mm is simulated. The plate is melted by a stationary laser with vertical incidence. The effective radius of the Gaussian-shaped laser source is 4 mm.

The calculation domain is an equidistant fixed grid of 60×40 square cells (constant axial and radial grid spacing of 0.15 mm) with the cylinder axis on the right boundary. The grid resolution has been chosen as a compromise between accuracy and computational costs. It is comparable to grid spacings used by Choo *et al.*[5,6] and Wang *et al.*,[9]

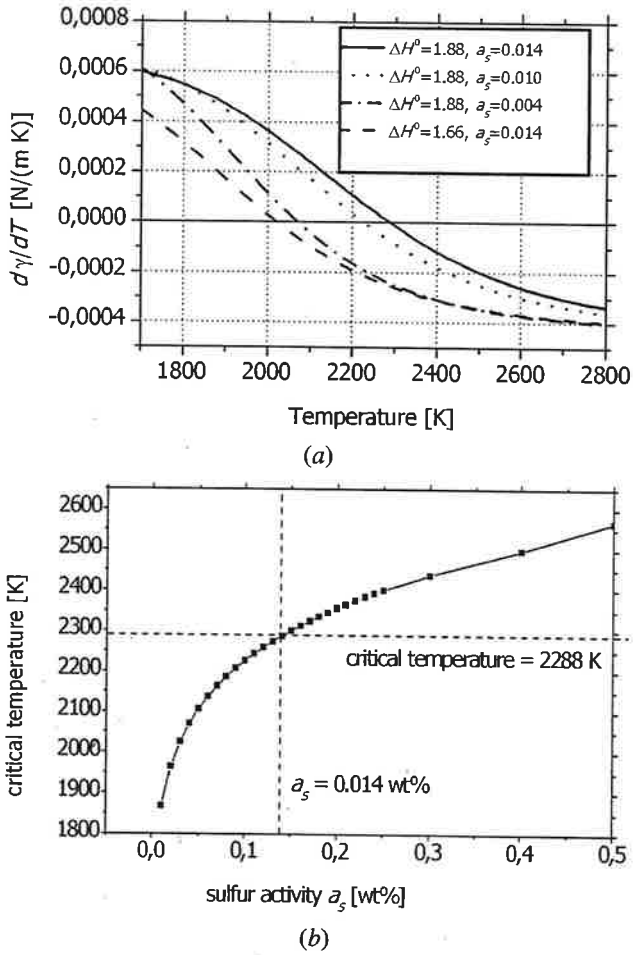

Fig. 2—(*a*) Dependence of Marangoni coefficient $\partial\gamma/\partial T$ on sulfur activity and standard heat of adsorption. (*b*) Dependence of critical temperature of Marangoni coefficient on sulfur activity. Both diagrams have been obtained by evaluation of Eq. [18].

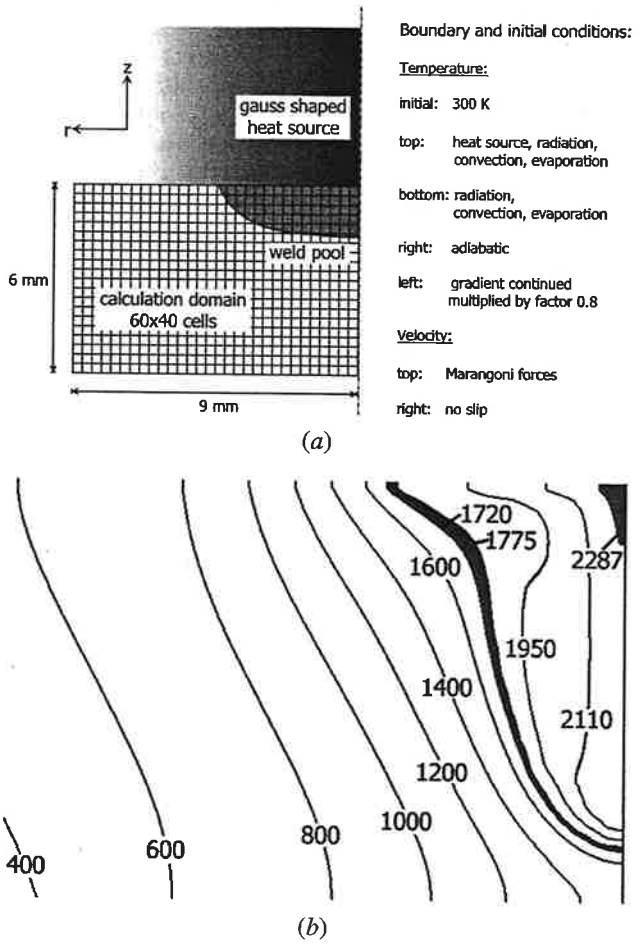

Fig. 3—(*a*) Set-up for the calculations, boundary and initial conditions; and (*b*) temperature scale, valid for all temperature plots. The gray area with temperatures above the critical temperature of the Marangoni coefficient, 2287 K, represents the area with a negative Marangoni coefficient, and the gray area with temperatures between 1720 and 1775 K represents the liquid-solid area or mushy zone for the initial composition.

who have performed extensive grid sensitivity trials and found that the accuracy of the results does not increase much with further refinement. An explanation might be that Marangoni convection is implemented as a momentum source term, so a finer grid would only increase the surface velocity, but not the total amount of momentum coupled into the melt. It seems that the increased surface velocities do not significantly affect the flow field deep in the pool. The use of a graded mesh in the area of the steepest temperature gradients did not appear to be reasonable, because in transient calculation, this area moves steadily outward.

The material used is the binary alloy Fe 0.42 wt pct C with constant sulfur content of 0.014 wt pct. Table I shows the material parameters and physical constants used for the calculations. To investigate the influence of constant surface parameters instead of temperature-dependent ones, a sensitivity analysis for the value of emissivity ε_b has been performed. Calculations with $\varepsilon_b = 0.2$ and $\varepsilon_b = 0.7$ did not show important changes in temperature distribution or pool shape.

Initially, the domain is set to $T = 300$ K. To simulate infinite dimension at the left boundary, the temperature gradients are continued, multiplied by a relaxation factor of 0.8. This is an empirically determined factor that ensures that the curvature of the isotherms does not change at the boundary. The initial time-step width is 0.001 seconds. Due to the high Marangoni flow velocities, this value sometimes had to be reduced by the adaptive time-step control down to 0.0002 seconds.

Each calculation was run on 4 of 26 processors of a SUN HPC 3500/6500 UltraSPARC-II system at the Edinburgh Parallel Computing Centre (EPCC, Edinburgh, Scotland), and took between 1 and 6 days to finish, depending on the molten area to be calculated.

E. *Definitions of Pool Shape Types and Characteristic Numbers: Preliminary Calculations*

A series of calculations were made to establish the influence of welding power on the pool shape. Before the results can be discussed, some definitions should be provided that help to describe and classify the results. The governing factor of the pool shape development is the time-dependent position of the critical temperature point on the surface where the Marangoni coefficient changes its sign. Areas with higher temperatures (in general, closer to the heat source) have a negative Marangoni coefficient, and areas with lower temperatures (further away) a positive one (Figure 2(a)). The main effect of this is that Marangoni-induced surface velocities are always directed toward the critical temperature point on the surface where the Marangoni coefficient changes its sign. Considering the series of calculations with different welding powers, two general types of pool shapes form if the welding duration is long enough.

If the welding power is low, the surface never reaches the critical temperature. Therefore, the Marangoni coefficient always remains positive and the surface flow is directed towards the middle of the pool (Figure 4(a)). The hot melt is redirected downward and results in a deep V-shape pool. Figure 5(a) shows the development of this pool type, including the resolidification phase when the laser has been switched off after 3 seconds, with $P = 1200$ W.

If the welding power is high, the surface reaches the critical temperature of the Marangoni coefficient quickly, and in the middle of the pool, the Marangoni coefficient becomes negative. This results in a violent outward flow. The fact that there is still a cooler surface area with a positive Marangoni coefficient that creates an adversary flow only starts having a major effect when the critical temperature point on the surface has reached the equilibrium position. From then on, the redirected hot melt from the two competing

Table I. Parameters and Physical Constants Used for the Calculations

$\alpha_{convection}$	convective heat-transfer coefficient	6.4 W/(m^2·K)
Γ_s	surface excess of the solute species (S) at saturation (Marangoni coefficient)	1.3×10^{-8} mol/m^2
ε_b	emissivity	0.2
λ_l	heat conductivity of liquid phase	27 W/(m·K)
λ_s	heat conductivity of solid phase	30 W/(m·K)
μ	dynamic viscosity of liquid phase	$6 \cdot 10^{-3}$ kg/(m·s)
ρ_l	temperature-dependent density of liquid phase	8547–0.835·T [kg/m^3]
ρ_s	constant density of solid phase	7344 kg/m^3
σ_b	Stefan–Boltzmann constant	$5.67 \cdot 10^{-8}$ W/(m^2·K^4)
A	$-\partial\gamma/\partial T$ for pure iron (Marangoni coefficient)	4.3×10^{-4} N/(m·K)
A_ν	constant for evaporation model (iron, evaporation model)	2.52
a_S	constant activity/concentration of surface active element sulfur (Marangoni coefficient)	0.014 wt pct
D_l	diffusion coefficient of carbon in liquid phase	$2 \cdot 10^{-9}$ m^2/s
h_l	temperature-dependent enthalpy of liquid phase	−25,394 + 790·T [J/(kg·K)]
h_δ	temperature-dependent enthalpy of solid δ phase	−149,502 + 706·T [J/(kg·K)]
h_γ	temperature-dependent enthalpy of solid γ phase	−108,636 + 675·T [J/(kg·K)]
ΔH_ν	specific evaporation heat (evaporation model)	6259.5 kJ/kg
ΔH^0	standard heat of adsorption (Marangoni coefficient)	-1.88×10^8 J/mol for AISI 304
r_{laser}	effective radius of the laser source	$4 \cdot 10^{-3}$ m
R	universal gas constant	8314.3 J/(mol·K)
S_l	constant, related to the entropy of segregation (Marangoni coefficient)	3.18×10^{-3}
T_a	ambient temperature	300 K
T_{max}	maximal surface temperature	2800 K

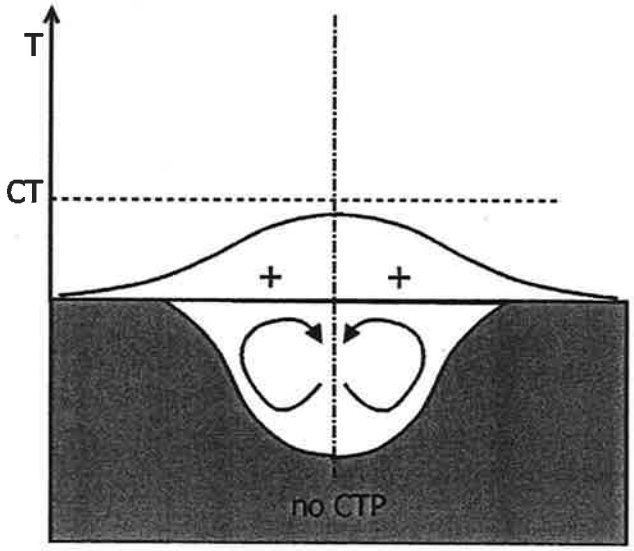

(*a*)

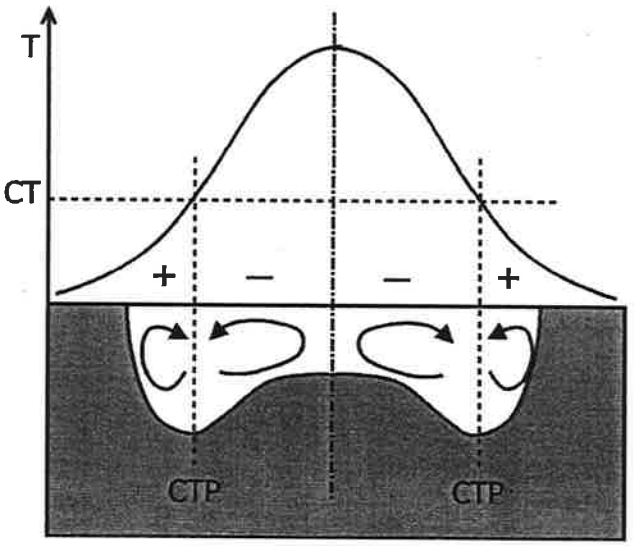

(*b*)

Fig. 4—Principal mechanisms that lead to the formation of (*a*) V-shape and (*b*) W-shape weld pools as a function of welding power. The Gaussian shape represents the temperature distribution on the surface; the position of the critical temperature point (CTP) on the surface where the Marangoni coefficient changes its sign governs the distribution of areas with positive (+) and negative (−) Marangoni coefficients.

adversary flows starts to form a second pool deepening, located beneath the critical temperature point (Figure 4(b)). This pool type is called W shape. Figure 5(b) shows the development of this pool type, including the resolidification phase when the laser has been switched off after 3 seconds, with $P = 2000$ W.

To be able to describe the development of the pool shape, some new quantities have been introduced. Corresponding to the usual habit of describing the weld pool shape by the depth/width ratio, the W-shape weld pool, and as a special case also the V-shape pool, is characterized here by a set of four numbers (Figure 6). All of them are geometric quantities normalized to a fixed reference radius R^{ref}, *e.g.*, the maximal pool radius of the calculation. The four quantities are

- the normalized central depth D_c/R^{ref} (in the middle of the pool);
- the normalized lateral depth D_l/R^{ref} (the depth of the second deepening, in general beneath the critical temperature point on the surface);
- the normalized offset O_l/R^{ref} of the critical temperature point; and
- the normalised radius R/R^{ref}.

In V-shape pools, the critical temperature point on the surface, where the Marangoni coefficient changes its sign, sometimes does not exist, because the surface never reaches the critical temperature. As the melt pool behavior in this case is similar to the behavior when the critical temperature point on the surface is situated in the middle of the pool, the two normalized depths are defined to be equal. This case can be difficult to interpret because it suggests the lateral deepening to be as deep as the central one. Therefore, the lateral depth should never be interpreted without considering the value of the offset of the critical temperature point. The lateral depth only gives additional information if the offset is different from zero.

When the laser is switched off, the critical temperature point shifts quickly toward the middle of the pool and then disappears. Nevertheless, the second deepening does not disappear that fast, but follows slowly. In this case, the lateral depth is defined as the maximal depth of the second deepening until it disappears and joins the central deepening.

III. APPLICATION TO LASER WELDING PROCESSES

A. *Influence of Welding Power on the Pool Shape*

In this study, we took into account laser welding calculations with a temperature-dependent Marangoni coefficient and welding powers $P = 1000$, 1200, 1300, 1395, 1500, 2000, and 4000 W. Figure 7 gives some examples for the weld pool shape, the temperature distribution, and the flow field after 2.5 seconds of welding time for different welding powers. Figures 8(a) through (c) show the time evolution of normalized central and lateral depth and the offset of the critical temperature point for different welding powers.

If the initial phase of pool formation is ignored, the calculations split into two groups forming V-shape or W-shape pools. With low powers (1000 to 1395 W), a stable V-shape pool is formed, and with high powers (1500 to 4000 W) a W shape is formed. The calculations with 1395 and 1500 W (and another calculation with 1400 W) crashed due to software problems: 1395 W after 1.05 seconds and 1500 W after 0.75 seconds. The exact reasons for the crashes are not fully understood, but a closer look at the initial pool development shows that between the power regions leading to a stable V or W shape formation, there is a critical power region (~1400 to 1500 W), where pool development shows a mixed, transient behavior. We assume that the complex flow patterns lead to difficult

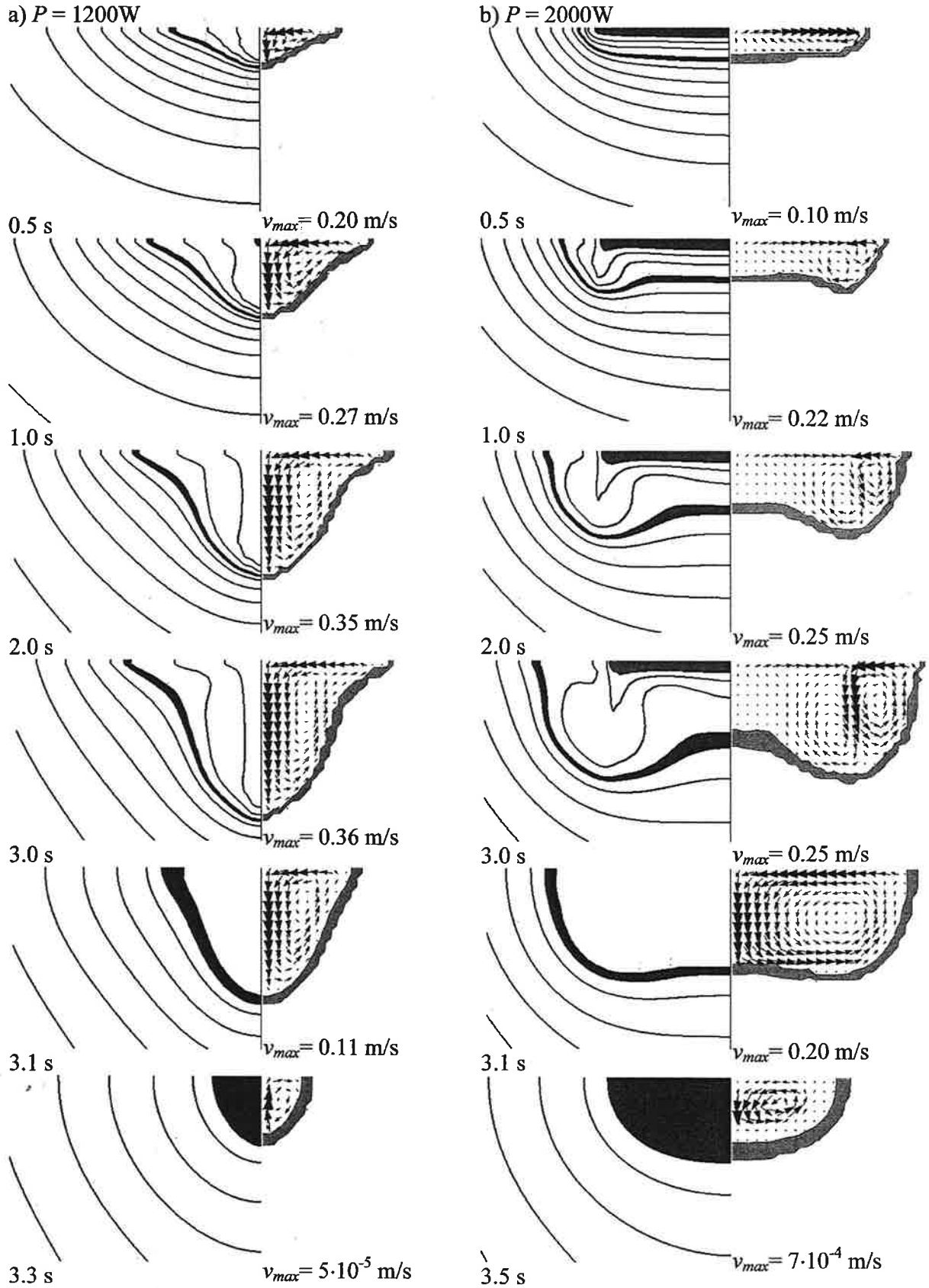

Fig. 5—Formation of different weld pool shape types (welding duration 3 s): (*a*) V shape (P = 1200 W), completely resolidified after 3.65 s; and (*b*) W shape (P = 2000 W), completely resolidified after 4 s. Left: temperature, scale given in Fig. 3(b); right: velocities, gray: mushy zone.

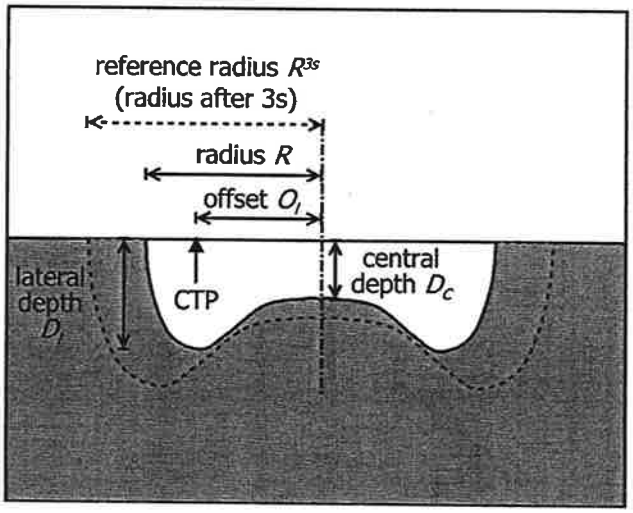

Fig. 6—Definitions of the quantities used to calculate the characteristic numbers for W-shape weld pools.

situations at the surface that cannot be handled correctly by the software.

A careful analysis of the time evolution of the weld pool shape (Figure 8) yields a number of interesting observations.

1. There is no smooth transition area between the areas with V- and W-shape behavior (Figure 9). For V-shape pools, the normalized central depth rather grows with rising power. The transition suddenly occurs in the critical power area. It is interesting to observe that this is not defined by the power where the surface first reaches the critical temperature of the Marangoni coefficient. In some calculations, with stable V-shape formation, an area with temperatures above the critical temperature appears, but it is not able to move far enough from the middle of the pool to help the pool establish a W shape. The transport of hot melt toward outer regions of the pool is prevented by the strong inward flow of cool melt. All calculations between $P = 1200$ and 1395 W show a predominance of the areas with positive Marangoni coefficient: For $P = 1200$ W, the surface reaches the critical temperature only from time to time; for $P = 1300$ W, a small region with temperatures above the critical temperature of the Marangoni coefficient is established; and for $P = 1395$ W, the hot melt tries to break out. The first calculation that probably manages to establish a W shape is the one with $P = 1500$ W. The calculations with higher powers show a critical temperature point on the surface that quickly shifts outward to reach a maximum offset and shifts back when the outer convection cell grows.
2. The calculations in the critical power range show a strong transient behavior. The calculation with $P = 1395$ W takes about 0.8 seconds to take its place in the series of V shapes from $P = 1000$ to 1300 W, and the calculation with $P = 1500$ W begins as a V shape and then starts to switch to W-shape behavior.
3. The comparison of the different characteristic numbers for one single welding power $P = 2000$ W (Figure 8(d)) shows more clearly the relation between central and lateral depth. It is obvious that the W shape only becomes visible when the lateral depth becomes larger than the central depth. The inverted situation at the beginning of the melting process ($t < 0.7$ seconds) and the maximum of the normalized offset of the critical temperature point are due to an interesting transient effect that will be described in Section B–2. The V-shape pools can be recognized from the central depth growing quickly and often after some time outrunning the radius. This would never occur with a W-shape pool.

B. *Transient Effects*

Consideration of the series of calculations gives strong evidence that transient effects play a major role in the development of the molten area during the heating process. Another important effect occurs after the laser has been switched off. Taking the case of $P = 2000$ W and welding duration of 3 seconds as an example, mainly three effects can be observed.

1. *Increasing central pool depth when the laser is switched off*

In W-shape pools, the molten area at the moment when the laser is switched off is not identical with the total molten area. In fact, the central pool depth still increases considerably after heating has stopped (Figure 10(a)). The effect is not limited to a certain welding duration. Calculations with $P = 2000$ W and durations of 0.5, 1.0, 1.5, 2.0, 2.5, and 3.0 seconds were made. All calculations that had enough time to form a W-shape pool showed the same effect. Only the calculation where the laser was switched off after 0.5 seconds, during the stage of the flat-shaped pool, did not grow deeper. The time evolution of the normalized radius shows that after 0.5 seconds the pool has not yet reached the stage of stable, regular W-shape growth (without figure).

The effect of increasing central depth is easy to understand. Figure 10(b) shows the situation shortly before and shortly after switching off the laser. Shortly before, the temperature distribution on the surface creates a stable W-shape pool. When heating stops, the surface starts to cool quickly. The critical temperature point on the surface shifts toward the middle of the pool and then disappears. Even if the temperature drops, the temperature distribution approximately keeps a Gaussian shape. The Marangoni coefficient that is now positive on the entire surface creates a Marangoni flow towards the middle of the pool, trying to transform the pool's W shape into a V shape. This process is stopped by solidification. Of course, the effect does not occur in V-shape pools because here, the Marangoni flow is already directed toward the middle of the pool, and when heating stops, the pool will only shrink.

Figure 11 shows the flow patterns during the first 0.3 seconds after the laser has been switched off and how the outer convection cell (surface flow toward the center of the pool) grows while the inner one is displaced and disappears.

The volume of the melt pool is not increased by this effect. When the laser is switched off, the molten area starts losing energy by conduction, radiation, and air convection. This energy loss results in a decreasing amount of liquid phase. Therefore, the melting process in the middle is

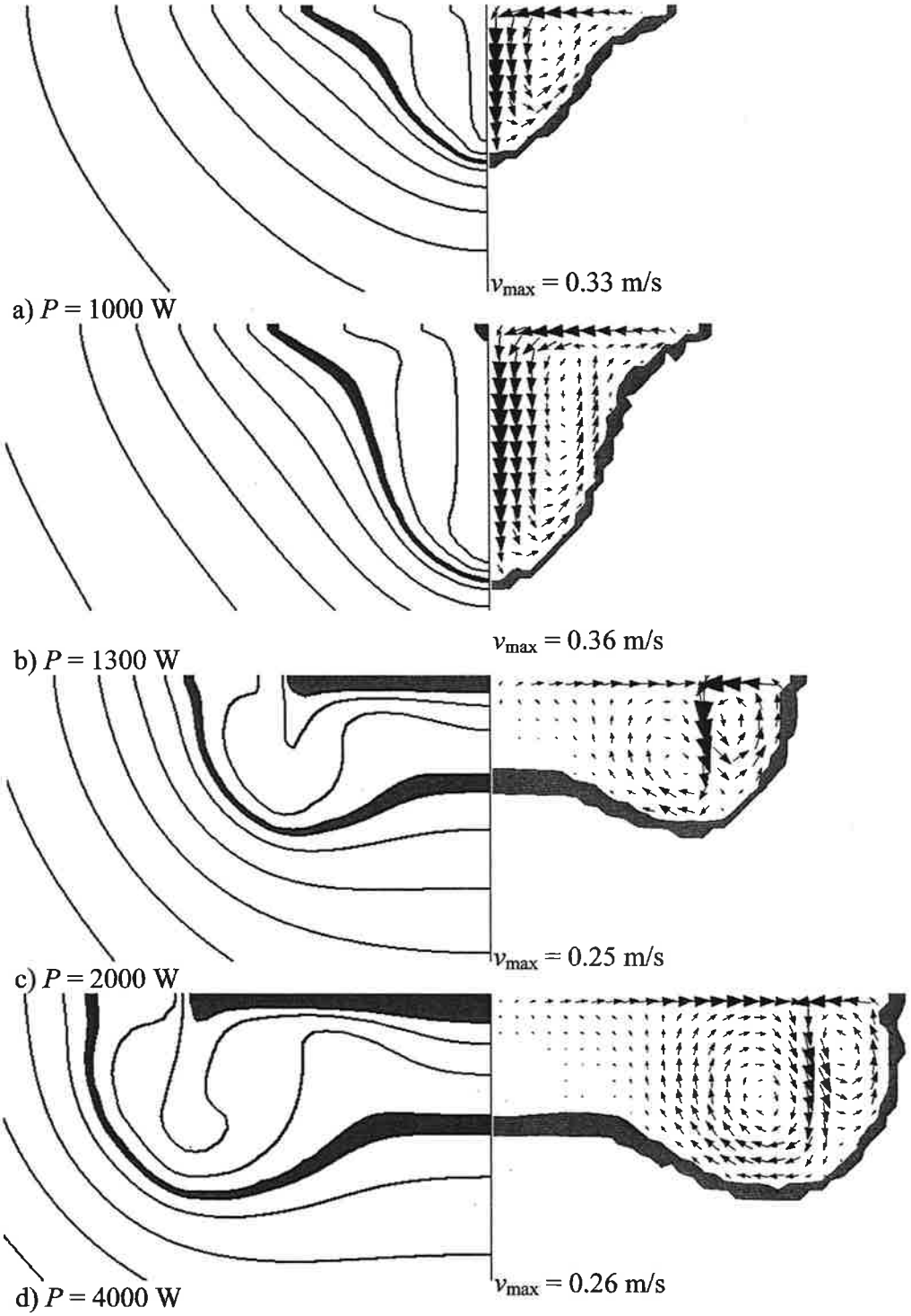

Fig. 7—Dependence of weld pool shape and depth on the welding power. Left: temperatures after 2.5 s, scale given in Fig. 3(b); right: velocities after 2.5 s, gray: mushy zone.

compensated by an increased solidification rate in the outer parts of the pool. Figure 10(c) shows the change of the pool shapes between the time when the laser is switched off and the time of the maximal central pool depth. The black areas are the additionally molten parts of the pool, while the gray areas represent the parts resolidified in the same time.

2. *Late formation of W shape*

The characteristic W shape does not develop from the beginning, but in a later stage of the melting process. Figure 12 shows the time evolution of a W-shape pool with $P = 2000$ W. First, the pool radius grows much quicker than the depth, forming a flat shape. The lateral deepening starts developing only when the critical temperature point on the surface reaches an equilib-

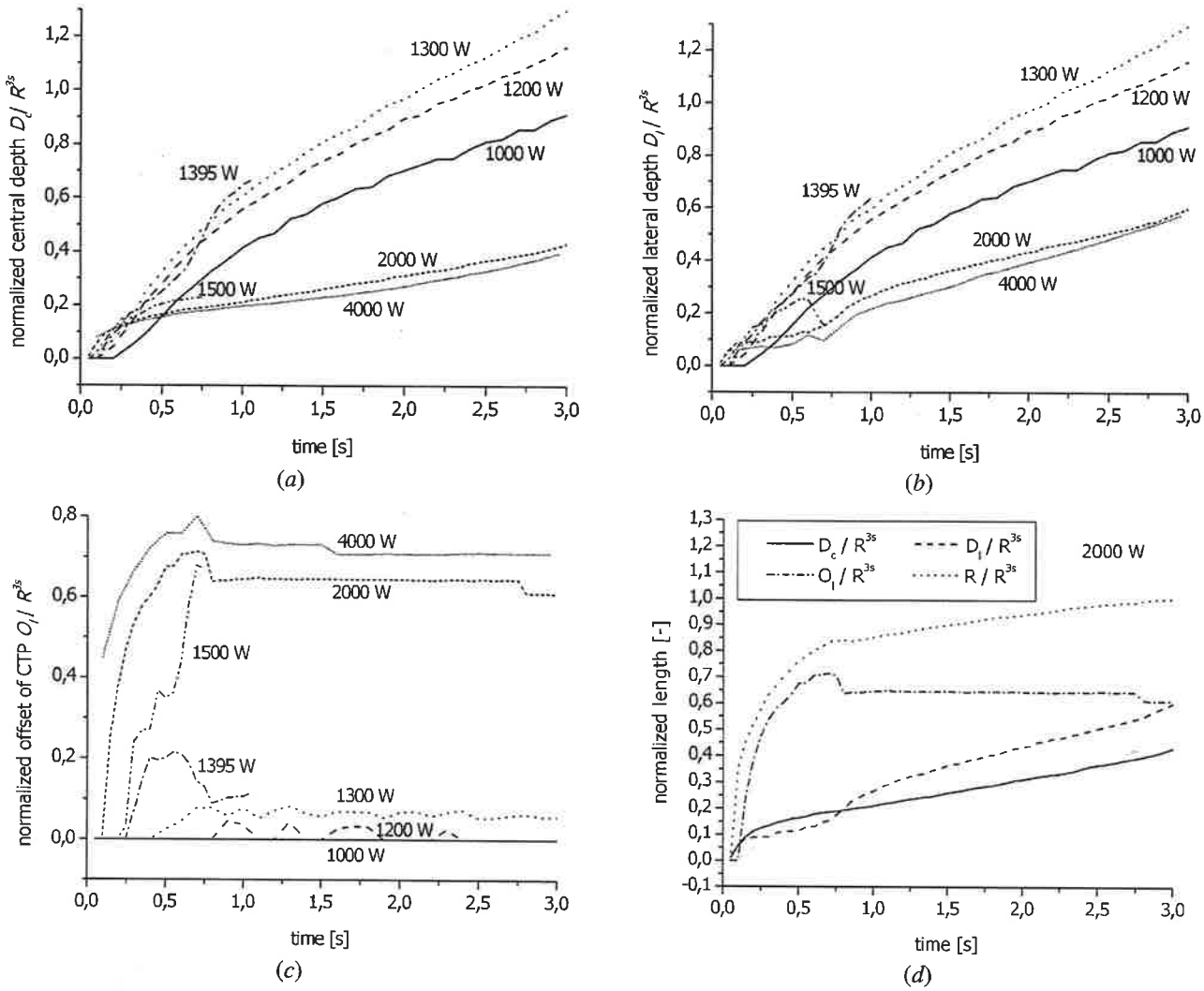

Fig. 8—(*a*) through (*c*) Time evolution of characteristic numbers for different welding powers: (*a*) normalized central depth D_c/R^{3s}; (*b*) normalized lateral depth D_l/R^{3s}; (*c*) normalized offset of critical temperature point O_l/R^{3s}; and (*d*) time evolution of all characteristic numbers for $P = 2000$ W.

rium position after 0.6 seconds. The reason for this is the quick heating. During the entire melting process, there is one area with a negative Marangoni coefficient in the middle that tries to enlarge the pool and a small, cooler area with a positive Marangoni coefficient at the outside that tries to slow down the enlargement. The two flows meet at the critical temperature point and are redirected downward. This mainly results in two competing convection cells and a deepening of the pool beneath the critical temperature point. At the beginning of the process, the critical temperature point moves quickly outward. The outer convection cell is small and the flow directed downward does not have time to deepen the pool significantly. When the critical temperature point reaches regions with weaker heat input by the welding source, the outer convection cell grows, and by the advection of cooler melt quickly stops the movement of the critical temperature point ($t = 0.6$ seconds). From now on, the lateral deepening of the W shape starts forming. When the outer convection cell grows, the critical temperature point is even pushed back toward the center of the pool. This effect has been observed in calculations with $P = 2000$ and 4000 W.

3. *Changing pool shape type in the critical power region*

In the critical power range between the two extreme behaviors of full W-shape formation for high powers and full V-shape formation (never reaching the critical temperature) for low powers, pool shape development is uncertain. In some cases the pool starts to develop W-shape behavior and later turns into a V shape. This is caused by the competition of opposed Marangoni forces on the surface. The temperature gradient distribution that governs the strength of Marangoni convection changes with time. One reason is the expansion of the Gaussian-shaped temperature profile, and a second is the alteration of the surface temperature by complex flow patterns of cool melt. This can result in a local reversal of the surface flow directions. Figure 13 shows two calculations with powers within the critical range. Both start developing a W-shape configuration but end up with different pool shape types. The 1395 W results in a V-shape pool and the 1500 W speeds up the pool enlargement showing the early stage of a typical W-shape formation (*cf.* Figure 12).

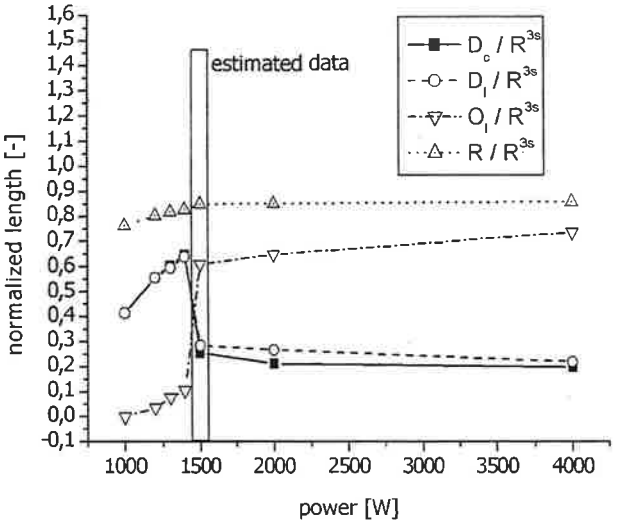

(*a*)

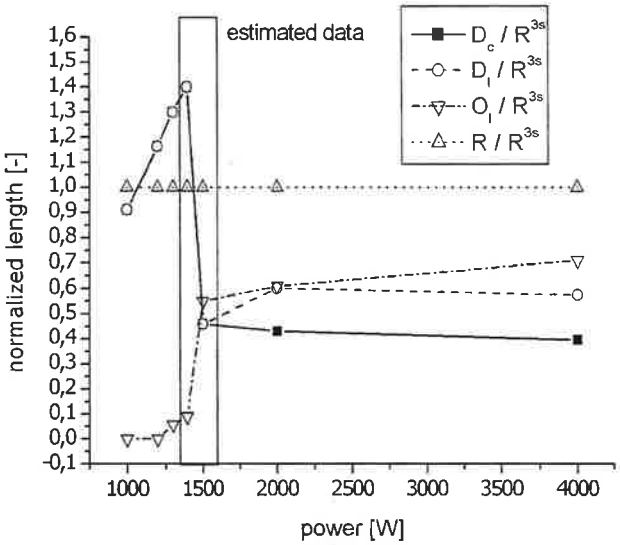

(*b*)

Fig. 9—Characteristic numbers of weld pools after (*a*) 1 s and (*b*) 3 s as a function of welding power.

C. *Discussion of Transient Effects*

The practical meaning of the effects described previously is of different quality.

1. The deepening of the pool after switching off the laser is mainly important for the comparison between numerical calculations and experiments. If the weld pool shapes found by steady-state calculations are compared to the shapes experimentally determined from micrographs, the transient effect can be responsible for considerable differences. Figure 10(d) shows these deviations, determined from the transient calculations.
   Of course, the calculations presented in this article have not been continued until reaching a steady state (which would be impossible anyway, as no artificial cooling was applied). The parameter study with different welding durations and the obvious explanation of the mechanism implies indeed that this effect will also occur under equilibrium conditions of a steady-state experiment/calculation, when the laser is switched off.
2. A quantitative knowledge of the W-shape formation could be used in the design of welding processes by determining minimum or maximum times for specific depth/width ratios or pool geometries wanted. If the characteristic times are well known for the material actually used, they could be used to determine the time when the laser has to be switched off.
3. At first sight, the unstable behavior of the pool shapes in the critical power region seems to be of minor importance, as the transient effect is quite small. One feature of the instable pool development is the formation of quite compact pool shapes in the initial phase. Of immense importance, however, is the quantitative knowledge of the position of the critical power region as a function of the concentration of surface-active elements. A direct regulation of concentration and welding power could thus be used in the design of specific welding processes.

IV. CONCLUSIONS

The numerical study of a special welding system has led to a set of general rules and remarks that can be used to understand and predict the dynamics and behavior of melt pools during laser welding.

1. If the concentration of surface-active elements allows the formation of a critical temperature point where the Marangoni coefficient changes its sign on the surface, the welding power range splits into three regions with (a) a pure V-shape behavior for the low powers, (b) unstable mixed V-W shape for a critical power region, and (c) pure W-shape behavior for high powers. For welding systems other than the one described in this work, *e.g.*, systems with higher or lower sulfur contents, completely other Marangoni parameters, or lower melting and evaporation temperatures, perhaps not all regions can be observed. The reasons may be as follows:
   a. The critical temperature of the Marangoni coefficient is too high to be reached, and therefore only the behavior of the low power range is observed; and
   b. The power is too high for the W shape to develop, and the pool would explode by evaporation (especially for Al alloys).

   In addition, with the central pool depth increasing after the laser has been switched off, a W shape that is observed on a micrograph becomes less distinct.
2. As for rising amounts of surface-active elements, the critical temperature of the Marangoni coefficient shifts to higher values; the position of the critical power range in this case rises too. The common observation that for constant welding powers the pool shape changes from a flat pool at low sulfur concentrations to deep pools at high concentrations is consistent with the fact that the sulfur concentration determines the value of the

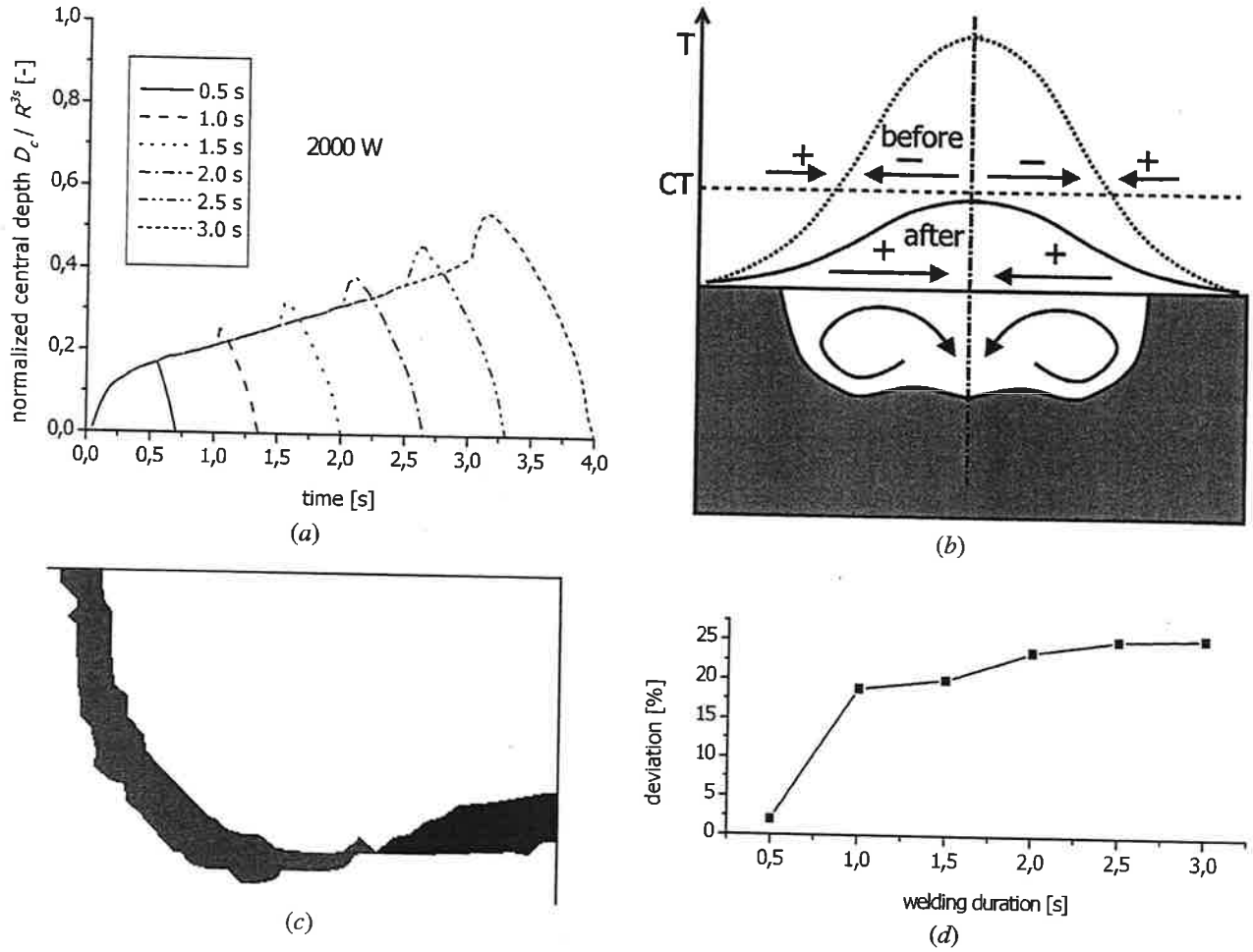

Fig. 10—Increase of normalized central depth after the laser (P = 2000 W) has been switched off; (*a*) time evolution of normalized central depth D_c/R^{3s} for different welding durations. (*b*) Principal mechanism explaining the increase of the central pool depth. The quick surface cooling makes the surface temperature drop under the critical temperature of the Marangoni coefficient and changes the Marangoni flow distribution from the case that has created the W shape to the case that would create a V-shape pool. (*c*) Development of the pool shapes between the time when the laser is switched off and the time of the maximal central pool depth; black: new molten area; gray: resolidified area. (*d*) Deviation in percent of central pool depths that would be measured from micrographs from "real" depths at the moment when the laser is switched off.

critical temperature of the Marangoni coefficient. For high sulfur activities, a certain power value could be in the V-shape region, while for low sulfur contents, it would be part of the W-shape region. A flat shape in this case might be due to a short welding duration preventing the W shape from forming. The position of the critical power region is further influenced by the value of the standard heat of adsorption, ΔH^0. The behavior of the Marangoni coefficient with changing parameter (Figure 2) implies no qualitative change of the pool shape behavior that would endanger the validity of the general rules.

3. The fact that the W shape cannot be observed in experiments with moving heat sources is due to three reasons.
   a. The projection of a moving W shape gives a flat pool shape. Even if the momentary pool is W shape, the traces are destroyed by the movement.
   b. In most cases, the effective local welding duration might be so short that the W shape does not have time to develop, and is stopped in the early stage with the flat shape.
   c. The 2-D axisymmetric solutions cannot simply be extrapolated to three-dimensional situations with moving laser sources, even if qualitative considerations strongly suggest the existence of competing areas with positive and negative Marangoni coefficients in whatever geometric situation, if the surface temperature reaches the critical temperature.
4. The experimental central pool depth that can be determined by evaluation of micrographs is, in the case of a W-shape pool, not identical with the central pool depth at the moment when the laser is switched off. This is due to the transient effect of a changing flow pattern, when the start of the cooling changes the distribution of the Marangoni coefficient on the surface. If steady-state calculations are compared with steady-state experiments, the error induced by this effect can be as much as 20 pct of the observed depth.

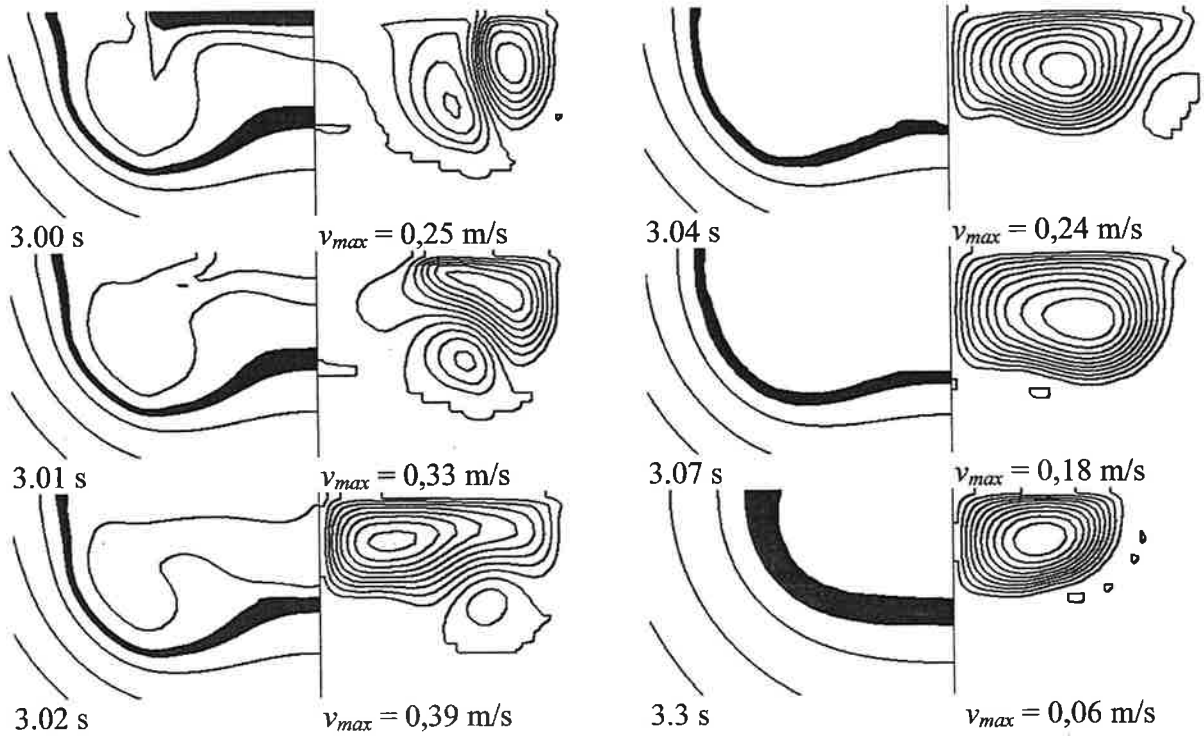

Fig. 11—Flow patterns that lead to an increased pool depth after switching off the laser at t = 3 s (P = 2000 W). Left: temperatures, scale given in Fig. 3(b); right: streamlines, the scales of different time-steps are not comparable. The strongest convection cell turns anticlockwise.

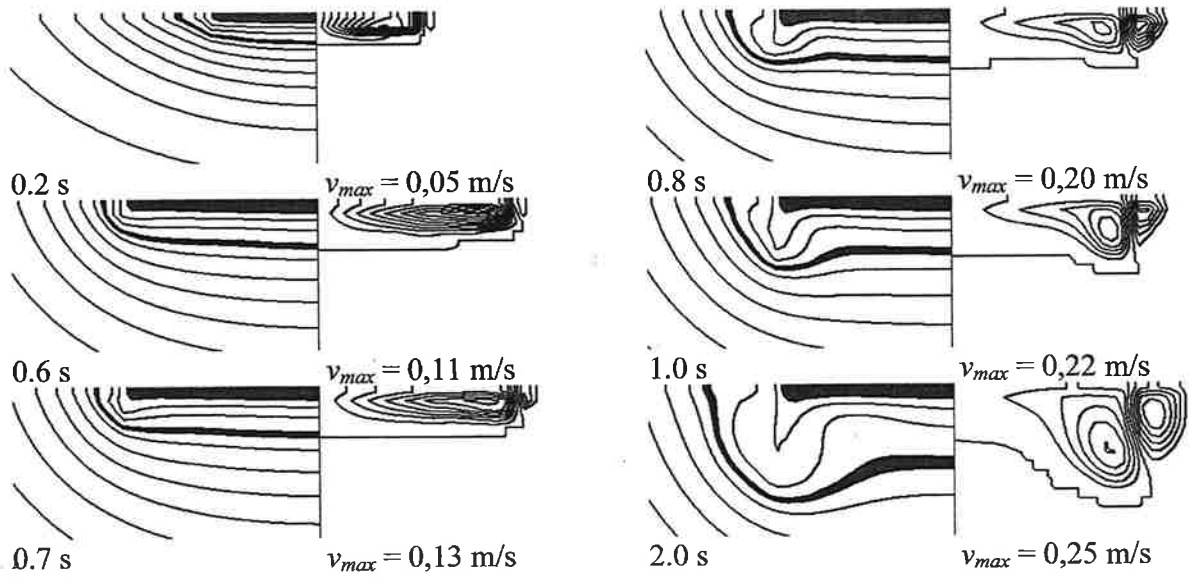

Fig. 12—Early stage in the evolution of W-shape pool (P = 2000 W); growth of flat pool between t = 0 and 0.6 s, formation of lateral deepening when the critical temperature point on the surface reaches equilibrium after 0.6 s. Left: temperatures, scale given in Fig. 3(b); right: streamlines, the scales of different time-steps are not comparable. The outer convection cells turn anticlockwise, and the inner ones turn clockwise.

5. The time evolution of W-shape pools shows two distinct phases, the quick formation of a flat pool in the early stage and the development of the full W shape later. A quantitative knowledge of this effect might help in the active design of welding processes by choosing ideal welding durations to obtain a special weld shape.
6. The weld pool dynamics in the critical power region during the initial phases leads to compact pool shapes that could also be used for weld pool design. One problem might be that the exact position of this region might be too difficult to determine and too unstable for practical applications.

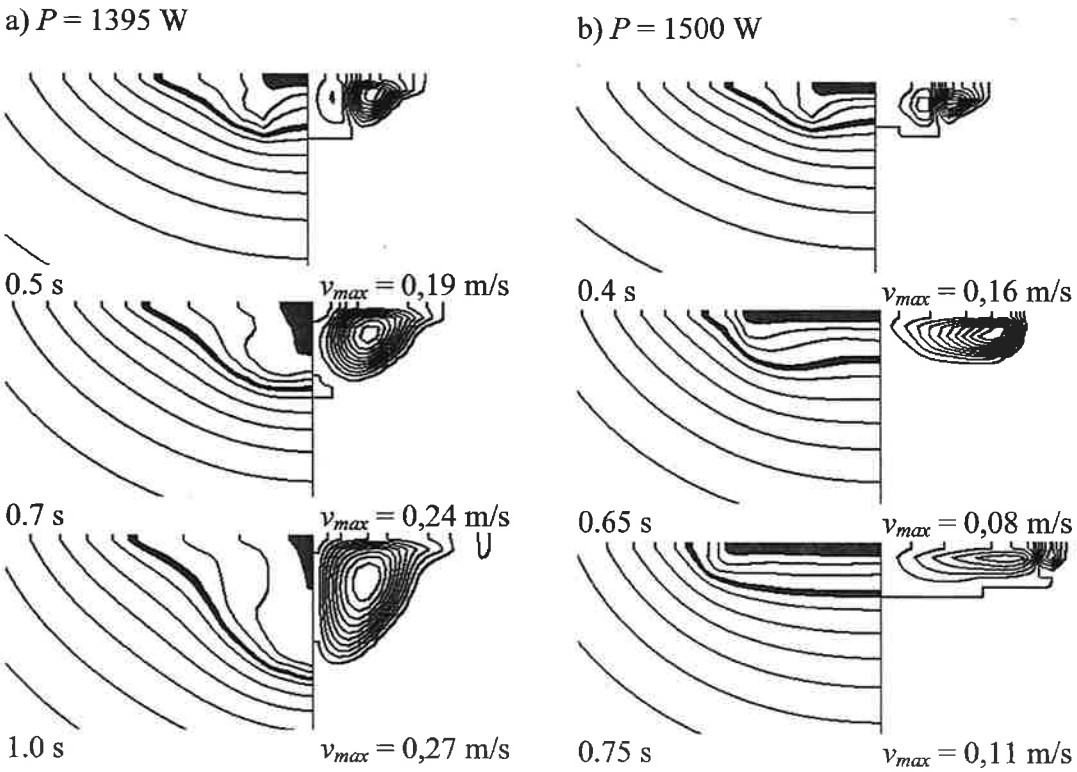

Fig. 13—Evolution of weld pool shape, temperature, and flow field for the initial phase of calculations in the critical power region: (*a*) $P = 1395$ W and (*b*) $P = 1500$ W. Both calculations start with comparable W-type pool shapes, but then develop into two different directions, V-shape type for $P = 1395$ W (outer convection cell becomes dominant) and flat initial phase of W-shape formation for $P = 1500$ W (inner convection cell becomes dominant). Left: temperatures, scale given in Fig. 3(b); right: streamlines, the scales of different time-steps are not comparable. The outer convection cells turn anticlockwise, and the inner ones turn clockwise.

The extrapolation of the results is of course limited by the assumption of a homogeneous and constant distribution of surface-active elements. Work by Winkler *et al.*[3] suggests that the distribution is strongly affected by the surface flow. This will result in a nonconstant value of the critical temperature of the Marangoni coefficient and thus in a more complex flow pattern.

Further work will concentrate on the systematic investigation of the interaction between Marangoni convection and electromagnetic forces in gas-tungsten-arc welding processes.

ACKNOWLEDGMENTS

This research was sponsored by the German Science Foundation DFG under Grant No. Sa 335/30 for which the authors express their gratitude. In addition, the authors acknowledge the support of the European Commission through IHP Grant No. HPRI-1999-CT-00026 (the TRACS programme at EPCC).

REFERENCES

1. J. Ni and C. Beckermann: *Metall. Trans. B*, 1991, vol. 22B, pp. 349-61.
2. S.V. Patankar: *Numerical Heat Transfer and Fluid Flow*, Hemisphere Publishing Corporation, New York, NY, 1980.
3. C. Winkler, G. Amberg, H. Inoue, and T. Koseki: in *Mathematical Modelling of Weld Phenomena 4*, H. Cerjak, ed., IOM Communications, London, 1998, pp. 37-69.
4. S. Kou and D.K. Sun: *Metall. Trans. A*, 1985, vol. 16A, pp. 203-13.
5. R.T.C. Choo and J. Szekely: *Welding Res. Suppl.*, 1992, mar., pp. 77s-93s.
6. R.T.C. Choo, J. Szekely, and S.A. David: *Metall. Trans. B*, 1992, vol. 23B, pp. 371-84.
7. K. Hong, D.C. Weckman, and A.B. Strong: *Trends in Welding Research*, Proc. 4th Int. Conf., June 5-8, Gatlinburg, TN, 1995, pp. 399-404.
8. V. Pavlyk and U. Dilthey: in *Mathematical Modelling of Weld Phenomena 5*, H. Cerjak, ed., IOM Communications, London, 2001, pp. 135-63.
9. Y. Wang, Q. Shi, and H.L. Tsai: *Metall. Trans. B*, 2001, vol. 32B, pp. 145-61.
10. C.R. Heiple and P. Burgardt: *Welding Res. Suppl.*, 1985, June, pp. 159s-62s.
11. W. Pitscheneder, T. DebRoy, K. Mundra, and R. Ebner: *Welding J. Res. Suppl.*, 1996, vol. 75 (3), pp. 71s-80s.
12. P. Sahoo, T. DebRoy, and M.J. McNallan: *Metall. Trans. B*, 1988, vol. 19B, pp. 483-91.
13. C. Prakash and H. Voller: *Num. Heat Transfer B*, 1989, vol. 15, pp. 171-89.
14. M.C. Schneider and C. Beckermann: "Summary of a Method for Numerically Simulating the Columnar Dendritic Solidification of Binary Alloys," Report No. UIME-CB01-1993, The University of Iowa, Iowa City, IA, 1993.
15. G. Ehlen, A. Ludwig, and P.R. Sahm: *Mater. Sci. Forum*, 2000, vols. 329-330, pp. 105-10.
16. T. Zacharia, S.A. David, and J.M. Vitek: *Metall. Trans. B*, 1991, vol. 22B, pp. 233-41.
17. Choi, R. Grief, and M. Salcuden: *Num. Heat Transfer*, 1987, vol. 11, p. 477.
18. S. Dushman: *Scientific Foundations of Vacuum Technique*, John Wiley & Sons, New York, NY, 1962.
19. C.S. Kim: "Thermophysical Properties of Stainless Steels," Report No. ANL-75-55, Argonne National Laboratory, Argonne, IL, 1975.